

A Kernel Space-based Multidimensional Sparse Model for Dynamic PET Image Denoising

Xiaodong Kuang^a, Bingxuan Li^b, Yuan Liu^c, Fan Rao^a, Gege Ma^a, Qingguo Xie^b,
Greta S P Mok^e, Huafeng Liu^d, Wentao Zhu^{a,*}

^aCenter for Frontier Fundamental Studies, Zhejiang Lab, Hangzhou, 310014, China

^bInstitute of Artificial Intelligence, Hefei Comprehensive National Science Center, 230000, Hefei, China

^cSchool of Electrical and Optical Engineering, Nanjing University of Science and
Technology, Nanjing, 210000, China

^dCollege of Optical Science and Engineering, Zhejiang University, Hangzhou, 310014, China

^eBiomedical Imaging Laboratory (BIG), Department of Electrical and Computer Engineering, Faculty of
Science and Technology, University of Macau, Macau, China

Abstract

Achieving high image quality for temporal frames in dynamic positron emission tomography (PET) is challenging due to the limited statistic especially for the short frames. Recent studies have shown that deep learning (DL) is useful in a wide range of medical image denoising tasks. In this paper, we propose a model-based neural network for dynamic PET image denoising. The inter-frame spatial correlation and intra-frame structural consistency in dynamic PET are used to establish the kernel space-based multidimensional sparse (KMDS) model. We then substitute the inherent forms of the parameter estimation with neural networks to enable adaptive parameters optimization, forming the end-to-end neural KMDS-Net. Extensive experimental results from simulated and real data demonstrate that the neural KMDS-Net exhibits strong de-

*Corresponding author

Email addresses: kuangxiaodong1991@gmail.com (Xiaodong Kuang),
libingxuan@iai.ustc.edu.cn (Bingxuan Li), liu_yuan_eo@163.com (Yuan Liu),
mvoofan@gmail.com (Fan Rao), gmgm590@163.com (Gege Ma), qgxie@ustc.edu.cn (Qingguo Xie),
gretamok@um.edu.mo (Greta S P Mok), liuhf@zju.edu.cn (Huafeng Liu),
zhuwentao.ee@gmail.com (Wentao Zhu)

noising performance for dynamic PET, outperforming previous baseline methods. The proposed method may be used to effectively achieve high temporal and spatial resolution for dynamic PET. Our source code is available at <https://github.com/Kuangxd/Neural-KMDS-Net/tree/main>.

Keywords:

Dynamic PET, Image denoising, Kernel, Sparse model, Neural network

1. Introduction

Positron emission tomography (PET) is widely used to evaluate the biological metabolism processes *in vivo* [1]. Due to various physical degradation factors and limited statistics, image reconstruction from PET data usually results in poor signal-to-noise ratio (SNR) and spatial resolution. Dynamic PET imaging may be more challenging when the counts become even lower for the early short frames when high temporal resolution is desired. Image denoising is important in order to acquired image frames with both high temporal and spatial resolution in dynamic PET.

Dynamic PET denoising methods may be divided into two categories, i.e., model-based and learning-based. The model-based methods include various denoising strategies within or after reconstruction. For reconstruction in dynamic PET, researchers have introduced various prior models for controlling image noise, such as edge preservation priors [2], voxel kinetics priors [3], anatomical priors [4] and kernel models [5]. Non-local means [6] and Highly constrained backProjection [7] are used to further improve the kernel methods. On the other hand, post-reconstruction denoising methods such as nonlocal mean filtering (NLM) [8], highly constrained backprojection (HYPR) processing [9], block matching and 3D filtering (BM3D) [10], image guided filtering

(IGF) [11] and wavelet denoising [12] have been proposed for dynamic PET. These model-based methods are physically interpretable. However, they heavily rely on the accuracy of system model, the choice of regularization terms, high-computational optimization and complex hyperparameter tuning.

The deep learning (DL)-based denoising methods have produced appealing results in computed tomography images [13] and multi-modal medical images [14] and have been successfully applied to dynamic PET. The convolutional neural network (CNN)-based methods such as population-based model [15] and three deep learning enhancement models [16] can effectively suppress noise yet may easily cause oversmoothed results. Generative Adversarial Networks (GANs) including dual GANs [17], conditional GANs [18] and cycle GANs [19] have been proposed to restore image details better, but the stability of training and the authenticity of generated details remain uncertain. Recently, denoising diffusion probabilistic model (DDPM) and score function-based model have been developed to learn the transition from a normal distribution to a specific data distribution, generating high-quality results that are virtually quite consistent with real data [20]. These methods directly learn the nonlinear mapping between the "noisy and clean" PET training data, ignoring the subjective physical mechanisms of PET imaging. Benefiting from their strong generalization ability, DL-based methods have demonstrated promising results when trained with a large amount of training data. However, their denoising performance may still be limited in complex clinical scenarios. To alleviate this issue, DL-based methods are incorporated into the image reconstruction process. For example, deep learning priors are used to accurately represent pixel features [21] and coefficient images [22] in kernel methods and also to

improve image quality in iterative reconstruction [23]. Although these methods have demonstrated strong generalization capabilities, the hyperparameter tuning and computational cost are usually challenging.

It is preferable to design a dynamic PET denoising method that combines the advantages of the model-based and DL-based approaches, i.e., with high interpretability and learnability. Kernel methods have been proven to effectively reduce noise in dynamic PET images. Its performance, however, relies heavily on the choice of hyperparameters, such as the kernel functions, composite images and search range in k -nearest neighbors (k NN). It has been reported that a trainable network can be used to automatically learn these hyperparameters in PET [24] and hyperspectral [25] image denoising. Moreover, the kernel methods usually take 3D images as input instead of 4D ones in previous literature, which does not fully exploit the spatial-temporal correlation. On the other hand, Qi *et al.* [26] proposed a N -order tensor which may be represented as a multidimensional signal to exploit the correlations in each dimension. Xiong *et al.* [25] applied this concept to construct a physical model in the image domain and used a network to learn the hyperparameters. Inspired by these previous works, we aim to introducing the kernel methods in the image domain and use multidimensional sparse coding to establish the relationship between temporal frames. Therefore in this paper, a model-based neural network is proposed for dynamic PET image denoising which integrates both the temporal and spatial image prior information, as shown in Fig. 1. Specifically, we build a kernel space-based multidimensional sparse (KMDS) model under the framework of multidimensional tensor sparse representation. The KMDS model has three steps. First, the noisy dynamic PET image is mapped into the ker-

nel space to obtain spatial-temporal correlations, yielding a kernel image. Second, the KMDS model uses a multidimensional tensor sparse model which sparsely encodes the kernel image with multidimensional dictionaries to reduce image redundancy. Finally, a denoised PET image is obtained through a linear combination of local pixels in the encoded kernel image. We then develop an end-to-end deep neural network named neural KMDS-Net, which substitutes each module in the optimization algorithm of the KMDS model with convolutional neural networks. Neural KMDS-Net consists of three stages, i.e., kernel representation, multidimensional sparse modeling, and image estimation.

This paper is organized as follows. Section II describes the proposed neural KMDS-Net. We then present the simulation studies in Section III and experimental results on real patient data in Section IV to demonstrate the advantages of neural KMDS-Net over other state-of-the-art model-based and DL-based methods. Finally, discussions and conclusions are drawn in Section V and VI.

2. Method

2.1. KMDS model formulation

Given a dynamic PET image frame \mathbf{y} with $M \times N \times Q$ pixels spatially and T frames, the observation model may be formulated as

$$\mathbf{y} = \mathbf{x} + \mathbf{n} \quad (1)$$

where $\mathbf{x} \in \mathbb{R}^{M \times N \times Q \times T}$ represents the true dynamic PET image to be estimated and $\mathbf{n} \in \mathbb{R}^{M \times N \times Q \times T}$ represents the additive noise. One common solution for the above problem

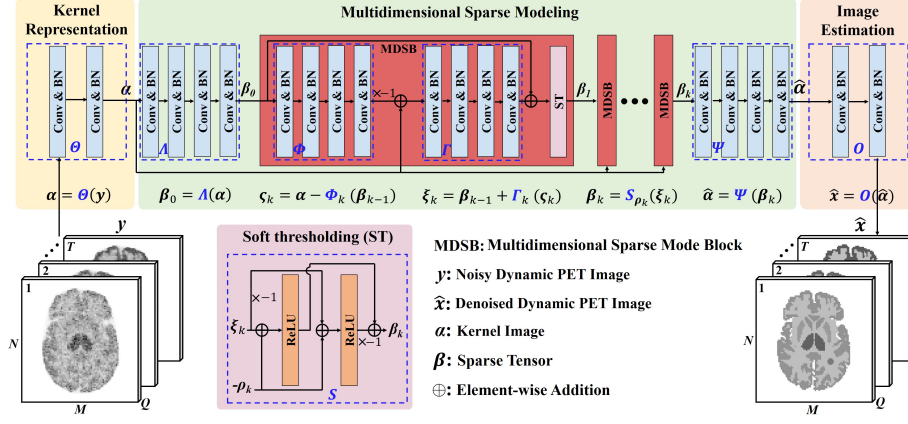


Figure 1: Illustration of the proposed method. First, the noisy PET image y is converted into the kernel representation α using the neural network Θ . The sparse representation β is then approximated from α using a series of multidimensional sparse coding blocks and used to compute the estimated kernel representation $\hat{\alpha}$. Finally, a neural network O is used to estimate the denoised PET image \hat{x} .

is to introduce prior information as regularization and then optimize the corresponding cost function.

As stated in [5], the image x can be represented by a kernel matrix $K \in R^{(MNQ) \times (MNQ)}$ and a coefficient image $\alpha \in R^{M \times N \times Q \times T}$

$$\tau(x) = K\tau(\alpha) \quad (2)$$

where $\tau(\cdot)$ represents the operation of transforming a matrix of size $M \times N \times Q \times T$ into a matrix of size $MNQ \times T$. K is typically obtained using composite images [5]. In this way, each pixel intensity in the image x is expressed as a linear function in the kernel space. Next, the prior knowledge of the correlations between any of 2 frames is used to model α .

For dynamic PET images, each frame $x_t \in R^{M \times N \times Q}$ has the same structure if motion

does not occur. \mathbf{K} is a pre-computed constant, implying that in the kernel space, each frame $\alpha_t \in \mathbb{R}^{M \times N \times Q}$ shares structural similarity. To exploit the correlations in every frame, we model α under the framework of multidimensional tensor sparse representation [26] as follows

$$\alpha = \beta \times_1 \mathbf{D}_1 \times_2 \mathbf{D}_2 \times_3 \mathbf{D}_3 \times_4 \mathbf{D}_4, \quad s.t. \|\beta\|_0 \leq S \quad (3)$$

where $\beta \in \mathbb{R}^{I_1 \times I_2 \times I_3 \times I_4}$ is a 4-order sparse tensor, $\mathbf{D}_1 \in \mathbb{R}^{M \times I_1}$, $\mathbf{D}_2 \in \mathbb{R}^{N \times I_2}$, $\mathbf{D}_3 \in \mathbb{R}^{Q \times I_3}$ and $\mathbf{D}_4 \in \mathbb{R}^{T \times I_4}$ are learned dictionary matrices, respectively. Here $I_1 \leq M$, $I_2 \leq N$, $I_3 \leq Q$, $I_4 \leq T$ and S is the sparsity indicating the number of non-zero elements in β .

Combining (1), (2) and (3), the proposed kernel space-based multidimensional tensor sparse coding problem is formulated as

$$\min_{\alpha, \beta} \frac{1}{2} \|\tau^{-1}(\mathbf{K}\tau(\alpha)) - \mathbf{y}\|_F^2 + \lambda_1 \left(\frac{1}{2} \|\alpha - \beta \times_1 \mathbf{D}_1 \times_2 \mathbf{D}_2 \times_3 \mathbf{D}_3 \times_4 \mathbf{D}_4\|_F^2 + \lambda_2 \|\beta\|_0\right) \quad (4)$$

where $\tau^{-1}(\cdot)$ represents the operation of transforming a matrix of size $MNQ \times T$ into a matrix of size $M \times N \times Q \times T$, the first term and the second term stand for the data-fitting terms in the original space and the kernel space, respectively. $\|\beta\|_0$ stands for the sparsity constraint term, λ_1 and λ_2 are parameters to control the fidelity and sparsity, respectively.

2.2. KMDS model optimization

Referencing [27], (4) can be optimized using a greedy approach, successively learning α from \mathbf{y} and sparse tensor β from α . Let \mathbf{K}^+ denote the pseudo-inverse matrix of \mathbf{K} , then α may be calculated by

$$\alpha = \tau^{-1}(\mathbf{K}^+ \tau(\mathbf{y})) \quad (5)$$

After obtaining α , next we optimize β . First, we relax the non-convex l_0 norm constraint in (4) to the l_1 norm to obtain a convex optimization problem as follows

$$\min_{\beta} \frac{1}{2} \|\alpha - \beta \times_1 \mathbf{D}_1 \times_2 \mathbf{D}_2 \times_3 \mathbf{D}_3 \times_4 \mathbf{D}_4\|_F^2 + \lambda_2 \|\beta\|_1 \quad (6)$$

Then this problem can be optimized using Tensor-based Iterative Shrinkage Thresholding Algorithm (TISTA) [26] by solving

$$\begin{aligned} \beta_k = S_{\lambda_2/L_k}(\beta_{k-1} - \frac{1}{L_k}(\beta_{k-1} \times_1 \mathbf{D}_1^T \mathbf{D}_1 \times_2 \mathbf{D}_2^T \mathbf{D}_2 \\ \times_3 \mathbf{D}_3^T \mathbf{D}_3 \times_4 \mathbf{D}_4^T \mathbf{D}_4 - \alpha \times_1 \mathbf{D}_1^T \times_2 \mathbf{D}_2^T \times_3 \mathbf{D}_3^T \times_4 \mathbf{D}_4^T)) \end{aligned} \quad (7)$$

where $S_{\lambda_2/L_k}(\cdot) = \text{sign}(\cdot) \max(|\cdot| - \lambda_2/L_k, 0)$ is the soft-thresholding operator, $L_k > 0$ is a Lipschitz constant and \mathbf{D}_i^T represents the transpose of \mathbf{D}_i . To update β , (7) can be rewritten as

$$\begin{aligned} \beta_k = S_{\lambda_2/L_k}(\beta_{k-1} + \frac{1}{L_k}(\alpha - \beta_{k-1} \times_1 \mathbf{D}_1 \times_2 \mathbf{D}_2 \\ \times_3 \mathbf{D}_3 \times_4 \mathbf{D}_4) \times_1 \mathbf{D}_1^T \times_2 \mathbf{D}_2^T \times_3 \mathbf{D}_3^T \times_4 \mathbf{D}_4^T) \end{aligned} \quad (8)$$

The optimization of β in (8) can be decoupled into three steps and sequentially connected to form a trainable network. Then, (8) becomes

$$\mathbf{s}_k = \alpha - \beta_{k-1} \times_1 \mathbf{D}_1 \times_2 \mathbf{D}_2 \times_3 \mathbf{D}_3 \times_4 \mathbf{D}_4 \quad (9)$$

$$\xi_k = \beta_{k-1} + \frac{1}{L_k} \mathbf{s}_k \times_1 \mathbf{D}_1^T \times_2 \mathbf{D}_2^T \times_3 \mathbf{D}_3^T \times_4 \mathbf{D}_4^T \quad (10)$$

$$\beta_k = S_{\lambda_2/L_k}(\xi_k) \quad (11)$$

The initialization of β can be set to $\beta_0 = \alpha \times_1 \mathbf{D}_1^T \times_2 \mathbf{D}_2^T \times_3 \mathbf{D}_3^T \times_4 \mathbf{D}_4^T$.

After computing β_k , $\hat{\alpha}$ can be obtained using the following formula

$$\hat{\alpha} = \beta_k \times_1 \mathbf{D}_1 \times_2 \mathbf{D}_2 \times_3 \mathbf{D}_3 \times_4 \mathbf{D}_4 \quad (12)$$

Finally, the denoised PET image $\hat{\mathbf{x}}$ can be obtained using (2).

The optimization of α and β mentioned above requires computationally inefficient iterations and complex fine-tuning of hyperparameters, such as λ_1 , λ_2 and L_k , which limit the generalizability of the KMDS algorithm. An alternative method is to unfold the iterative optimization steps of β as network layers to automatically learn the sparse dictionaries and hyperparameters [25]. However, there are noticeable differences in image quality and quantitation across frames of dynamic PET. This makes simple dictionary matrices with limited representation ability unable to address the challenging issue, resulting in obvious noise and bias in the shorter scan denoised using [25] directly. In addition, the kernel matrix \mathbf{K} of an image is usually too large to calculate its pseudo-inverse \mathbf{K}^+ . To address these issues, we propose a neural KMDS-Net, as described in the next section.

2.3. Neural KMDS-Net

The kernel representation $\tau^{-1}(\mathbf{K}^+\tau(\mathbf{y}))$ of \mathbf{y} in (5) may be generalized to multiple image convolutions using learned local filters, i.e.

$$\alpha = \mathbf{y} \circ \mathbf{c}_1^n \circ \mathbf{c}_2^n \circ \dots \circ \mathbf{c}_m^n \quad (13)$$

where $\mathbf{y} \circ \mathbf{c}_i^n = \mathbf{c}_i^n(\mathbf{y})$, \mathbf{c}_m^n denotes the m -th convolutional layer with output filter number n . To prevent gradient explosion, batch normalization (BN) [28] layer is added after each convolution layer. Let \mathbf{b}_m represent the m -th BN layer, we have

$$\alpha = \boldsymbol{\Theta}(\mathbf{y}) \quad (14)$$

where $\boldsymbol{\Theta}(\mathbf{y}) = \mathbf{y} \circ \mathbf{c}_1^n \circ \mathbf{b}_1 \circ \mathbf{c}_2^n \circ \mathbf{b}_2 \circ \dots \circ \mathbf{c}_m^n \circ \mathbf{b}_m$.

Considering the strong representation ability of DL, we use convolutional neural networks to substitute dictionary matrices to improve the performance of KMDS method by learning the sparse representation β from α more accurately. Then, (9)-(11) generalize to the following form

$$\mathcal{S}_k = \alpha - \Phi_k(\beta_{k-1}) \quad (15)$$

$$\xi_k = \beta_{k-1} + \Gamma_k(\mathcal{S}_k) \quad (16)$$

$$\beta_k = S_{\rho_k}(\xi_k) \quad (17)$$

where Φ_k and Γ_k both represent a CNN with four cascaded convolutional layers. A BN layer is added after each convolutional layer. Each convolutional layer corresponds to a dictionary matrix. $1/L_k$ is implicitly merged to Γ_k . $\rho_k \in R^{1 \times 1 \times 1 \times L_4}$ denotes the soft thresholding parameter tensor for the k -th iteration optimization of the parameter β . The soft-thresholding operator can be written as $S_{\rho_k}(\xi_k) = \max(\xi_k - \rho_k, 0) - \max(-\xi_k - \rho_k, 0)$. $\max(\cdot)$ can be replaced by a rectified linear units (ReLU) layer, and we have $S_{\rho_k}(\xi_k) = \text{ReLU}(\xi_k - \rho_k) - \text{ReLU}(-\xi_k - \rho_k)$. Furthermore, the dictionary matrices used in the initialization of β_0 may also be substituted with convolutional layers. We have $\beta_0 = \Lambda(\alpha)$, where Λ and Φ_k share the same network architecture. Therefore, the optimization of the sparse representation β may be implemented by a fully convolution neural network which may achieve better results by implicitly embedding explicit parameters into the neural network training process. We compose (15), (16) and (17) into a multidimensional sparse block (MDSB) and stack it for k times to form a sub-network for multidimensional sparse coding.

After obtaining β_k , $\hat{\alpha}$ in (12) may also be represented by a neural network as follows

$$\hat{\alpha} = \Psi(\beta_k) \quad (18)$$

where Ψ , similar to Φ_k , is also a four-layer CNN. Finally, the kernel matrix \mathbf{K} in (2) may also be replaced by multiple convolutional layers. The denoised $\hat{\mathbf{x}}$ may be obtained by

$$\hat{\mathbf{x}} = \mathbf{O}(\hat{\alpha}) \quad (19)$$

where $\mathbf{O}(\hat{\alpha}) = \hat{\alpha} \circ \mathbf{d}_1^n \circ \mathbf{b}_1 \circ \mathbf{d}_2^n \circ \mathbf{b}_2 \circ \dots \circ \mathbf{d}_m^n \circ \mathbf{b}_m$ and \mathbf{d}_m^n denotes the m -th convolutional layer with output filter number n . We refer to this model as the neural KMDS-Net. The network architecture is shown in Fig. 1.

2.4. Network training loss

The mean squared error (MSE) between the output $\hat{\mathbf{x}}$ of neural KMDS-Net and the reference image \mathbf{x} is used to form the training loss function

$$L = \|\hat{\mathbf{x}} - \mathbf{x}\|_2^2 \quad (20)$$

2.5. Evaluation metrics

Peak signal-to-noise ratio (PSNR) and the structural similarity (SSIM) are used to compare different image denoising methods. The ensemble bias of the mean intensity and background normalized standard deviation (NSD) in regions of interest (ROIs) are also computed to evaluate ROI quantification and measure the noise,

$$\text{Bias} = \frac{|\bar{c} - c^{\text{true}}|}{c^{\text{true}}} \quad (21)$$

$$\text{NSD} = \frac{1}{N_r} \sum_{i=1}^{N_r} \frac{1}{\bar{b}_i} \sqrt{\frac{1}{N_b - 1} \sum_{j=1}^{N_b} (b_{i,j} - \bar{b}_i)^2} \quad (22)$$

where c^{true} is the noise-free intensity and $\bar{c} = \frac{1}{N_r} \sum_{i=1}^{N_r} \bar{c}_i$ denotes the mean of N_r realizations. \bar{c}_i is the mean ROI uptake in the i -th realization and $N_r = 10$ in this study. $b_{i,j}$ is the j -th voxel intensity of the background ROI in the i -th realization. \bar{b}_i is the mean voxel intensity and N_b denotes the number of voxels in the background ROI.

2.6. Implement details

Neural KMDS-Net is implemented in Pytorch and trained on a NVIDIA Tesla V100 GPU. The training images at different frames are divided by their maximum voxel values. The Adam algorithm is used with a initial learning rate 5×10^{-3} , which is multiplied by 0.35 for every 80 epochs. The batch size is 2 and the model is trained for 300 epochs until convergence. 3D convolutional layers and 3D BN are used in neural KMDS-Net. Each convolutional layer in neural KMDS-Net is with kernel size 3, stride 1 and padding 1. The network’s input and output are tensors of size $B \times T \times Q \times M \times N$, where B represents the batch size. m and n in (13) and (19) are set to 2 and T , respectively. The number of input and output channels for each convolutional layer in \mathbf{A} , Φ_k , Γ_k and Ψ is set to T . The number of unfolding k is set to 20. The model size of neural KMDS-Net in simulation and real studies is 10.5 M and 14.2 M respectively.

2.7. Reference methods

We compare the proposed neural KMDS-Net with the standard ML-EM method, the kernelized expectation maximization (KEM) method [5], the ResNet direct denoising method [29], the Pix2Pix-based generative adversarial network (GAN) direct denoising method [30], the subspace-based multidimensional sparse (SMDS)-Net iterative unrolling network method [25] and the DDPM-PET method [20]. In the KEM

method, three 20-minute composite frames are used as the prior images. σ is set to 1 in the radial Gaussian kernel function and the number of nearest neighbors is set to 50 in k NN to generate the sparse kernel matrix \mathbf{K} . For the ResNet direct denoising method, the number of output filters in the first convolutional layer is set to 32 and the number of residual block is set to 9. In the Pix2Pix-based GAN, the generator uses the same ResNet structure mentioned above and the number of output channels for the first convolutional layer of the discriminator is 64. The input noisy image is added to the discriminator as a conditional term. The weight for the discriminator loss is empirically set to 0.03 based on our previous work [31] and experimental analysis. 3D convolution layers and 3D BN are used in ResNet and GAN. The DDPM-PET method only uses the PET images as the input for the network and is implemented using the modified open-source PALETTE framework [32]. The batch size is set to 16. The base channel count is set to 32 and the number of residual blocks is set to 1. Other model parameters are configured to be consistent with the parameters for the colorization task. The SMDS-Net method is implemented through the open-source code provided by the authors. Some parameters, such as patch size ($M \times N$), cube size ($[5, 5, 5]$), number of dictionaries ($[9, 9, 9]$) and unfolding numbers (3), are reconfigured to achieve better results in dynamic PET image denoising.

3. Simulation validation

3.1. Simulation setup

Dynamic ^{18}F -FDG scans are simulated for a PET/CT scanner using a $128 \times 128 \times 8$ Zubal head phantom as shown in Fig. 2. The phantom is composed of gray matter,

Table 1: The mean values of the simulated kinetics parameters for different organs. V stands for blood volume ratio.

	K_1	k_2	k_3	k_4	V
Gray matter	0.080	0.140	0.170	0.013	0.103
White matter	0.050	0.110	0.050	0.006	0.026
Caudate	0.070	0.170	0.190	0.016	0.101
Putamen	0.090	0.160	0.170	0.010	0.092
Thalamus	0.110	0.160	0.140	0.012	0.152
Tumor	0.130	0.100	0.150	0.015	0.173

white matter, caudate, putamen, thalamus and a tumor. The sampling protocol is set to 24 time frames: $4 \times 20s$, $4 \times 40s$, $4 \times 60s$, $4 \times 180s$, and $8 \times 300s$.

The time activity curves (TAC) of different regions are generated using a three compartmental model with a blood input function. For data augmentation, each kinetic parameter follows a Gaussian variable with coefficient of variation equal to 20% of the mean values. The mean values of kinetic parameters are shown in Table 1. The TACs using the mean kinetic parameters are shown in Fig. 2. The total number of events over 1 hours is 1.19 billion. Translation and scaling are applied to the phantom for data augmentation. The ground-truth images are first forward-projected to generate noise-free sinograms. Poisson noise is then introduced. The random and scatter events are simulated using Monte Carlo simulation and account for approximately 30% statistics of the noiseless data. For the training data, we generate 2000 noisy-clean PET image pairs, with each image being of size $128 \times 128 \times 8 \times 24$. For the test data, in total 600 (60×10) pairs are generated, with 10 noisy realizations simulated for each true image.

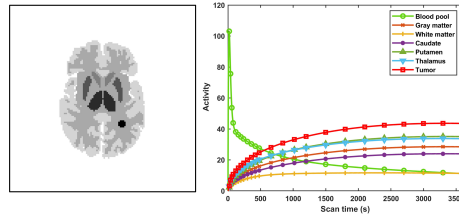


Figure 2: The Zubal brain phantom (left) and examples of time activity curves (right) used in the simulation studies.

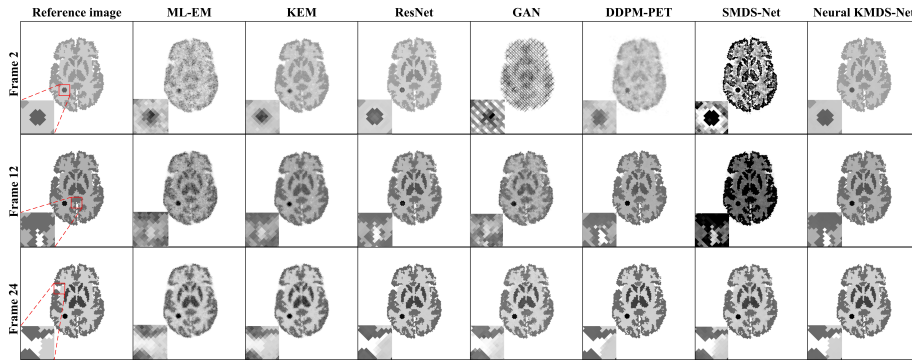


Figure 3: True activity images and denoised images by different denoising methods in the simulation study. The window size of frame 2 (top row), frame 12 (middle row) and frame 24 (bottom row) is set to $[0, 0.01]$, $[0, 0.1]$ and $[0, 1.0]$, respectively.

3.2. Comparison of Image Quality

Fig. 3 shows the ground-truth images and the denoised images by seven different methods for frame 2, frame 12 and frame 24 in the simulation. It may be observed that ML-EM has the highest noise among all. The regular KEM achieves better results compared to ML-EM. ResNet suppresses noised well and preserves fine details. GAN yields very poor results for frame 2 due to the significant differences in pixel intensity distribution between frames, which exacerbated the difficulty of the model's learning process. For frame 2, DDPM-PET is noisier than ResNet. SMDS-Net yields

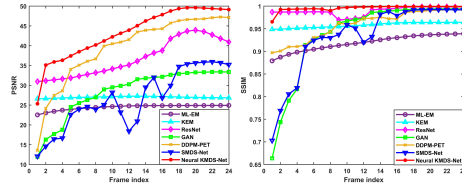


Figure 4: Plots of image PSNR and SSIM of all time frames for different denoising methods.

Table 2: Quantitative comparison of different organs by different methods in frame 2 and 24 from the simulation study. Mean PSNR is reported. Best results are marked in **BOLD**.

Local PSNR	Gray matter		White matter		Caudate		Putamen		Thalamus		Tumor	
	2	24	2	24	2	24	2	24	2	24	2	24
ML-EM	31.919	32.675	26.216	28.486	28.622	31.083	38.714	40.125	37.191	38.453	34.714	38.110
KEM	32.564	34.395	31.589	30.892	33.806	32.632	40.637	41.348	41.768	40.571	37.232	39.741
ResNet	42.473	55.042	35.498	46.339	39.105	47.854	49.134	57.286	44.261	53.892	42.169	52.777
GAN	28.598	52.911	19.585	35.603	19.777	42.125	34.369	47.669	31.743	45.195	29.121	43.698
DDPM-PET	31.780	56.929	28.303	50.809	30.110	53.891	41.318	60.734	39.622	59.685	37.672	60.957
SMDS-Net	26.981	45.924	7.401	38.833	14.423	40.547	20.575	48.806	17.481	49.987	16.004	47.962
Neural KMDS-Net	55.654	63.776	39.864	52.535	42.014	54.660	49.467	64.130	50.223	63.181	45.412	63.035

significantly biased results for frame 2 and frame 12 partially due to the limited learning capacity of the dictionary matrix. In comparison, benefiting from the interpretable neural network, the proposed neural KMDS-Net achieves the best image quality and demonstrated best detail preservation.

Fig. 4 further shows quantitative assessment for all time frames denoised by different methods. We may observe that the neural KMDS-Net is with a higher PSNR for frame 1 and outperforms all compared baselines in terms of PSNR and SSIM for other frames. The quantitative assessment of six organs using different methods for frame 2 and frame 24 is summarized in Table 2. The neural KMDS-Net shows a significant improvement in PSNR over other methods in all organ ROIs.

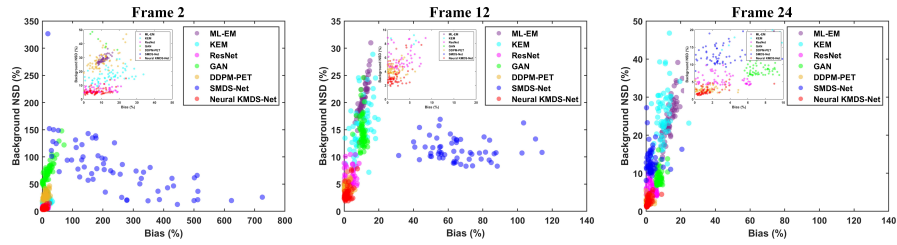


Figure 5: Plots of bias-NSD for tumor ROI quantification in frame 2, 12 and 24. White matter is selected as the background to compute NSD. A zoom-in is included for each frame.

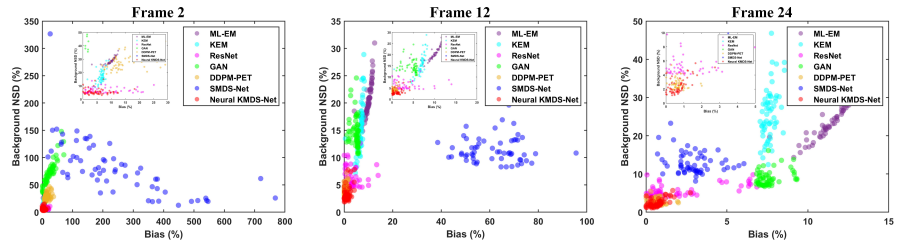


Figure 6: Plots of bias-NSD for gray matter ROI quantification in frame 2, 12 and 24. White matter is selected as the background to compute NSD. A zoom-in is included for each frame.

3.3. Comparison of ROI quantification

Figs. 5-6 show the trade-off between the absolute bias and NSD of different methods for ROI quantification in the tumor (Fig. 5) and gray matter (Fig. 6) regions. Each point is obtained by calculating the average of the denoising results from 10 noisy realizations of a test image. For both the tumor ROI and gray matter quantification, SMDS-Net is with the highest bias in frame 2 and frame 12 but performs better than the GAN, KEM and ML-EM in frame 24. DDPM-PET demonstrates a remarkable superiority in frame 12 and frame 24 compared to other regular DL methods and traditional approaches. However, it exhibits relatively higher background noise in frame 2 compared to the KEM, ResNet and the proposed method. In comparison, the proposed neural

Table 3: The PSNR of different depth m of neural networks in kernel representation and image estimation modules. Best results are marked in **BOLD**.

m	0	2	4	6	8	10	12
Frame 2	32.43	35.05	33.68	33.36	31.31	30.82	33.23
Frame 12	40.74	42.11	40.48	39.67	39.64	39.67	38.93
Frame 24	44.05	45.22	45.06	44.63	45.40	44.54	44.64

Table 4: The PSNR of different unfolding iteration k on the simulated dataset. Best results are marked in **BOLD**.

k	5	10	15	20	25	30
Frame 2	34.10	34.72	32.87	35.05	33.63	32.34
Frame 12	40.31	41.07	41.20	42.11	39.65	42.04
Frame 24	42.18	43.82	44.26	45.22	45.69	46.35

KMDS-Net achieves the best bias-NSD trade-off among the other reference methods.

3.4. Network optimization

Here we conduct an ablation study on our neural KMDS-Net to show the strong learning ability. All experiments are conducted on the Zubal head dataset.

3.4.1. Parameter m

We change the depth m of neural networks in (13) and (19) from 0 to 12 with an interval of 2. The number of 0 indicates that neural KMDS-Net does not include kernel representation and image estimation modules. As shown in Table 3, increasing the depth of neural networks does not always allow for better denoising performance. This may be attributed to the straightforward concatenation architecture of neural networks. Therefore, the parameter m is set to 2 considering the denoising performance.

Table 5: The PSNR of different sizes of β on the simulated dataset. Best results are marked in **BOLD**.

I_1, I_2, I_3	I_4	Frame 2	Frame 12	Frame 24
$64 \times 64 \times 4$	12	32.54	37.74	41.65
	16	33.32	37.84	43.28
	20	31.50	38.29	43.29
	24	33.62	39.39	44.83
	28	32.54	40.11	44.09
	32	31.41	38.28	44.14
$128 \times 128 \times 8$	12	34.05	40.69	44.31
	16	33.58	41.58	45.24
	20	33.34	41.37	44.66
	24	35.05	42.11	45.22
	28	32.45	41.00	44.05
	32	32.06	41.93	46.41

3.4.2. Unfolding iteration k

k denotes the number of iterations for the parameters updates in (15) to (17) and also controls the depth of the neural network modules of multidimensional sparse representation. Table 4 shows the influence of the unfolding iteration k . A larger k enforces the network to take advantage of the information between current iteration and historical iterations to optimize the parameters, implying that larger number should be chosen. However, increasing k from 20 to 30, the denoising performance does not show a significant improvement. Considering the tradeoff between the inference time and denoising performance, k is set as 20.

3.4.3. Different sizes of β

Here, we analyze the influence of the size of sparse tensor β in multidimensional sparse coding on dynamic PET denoising. For simplicity, we set $I_1 = I_2$ and choose

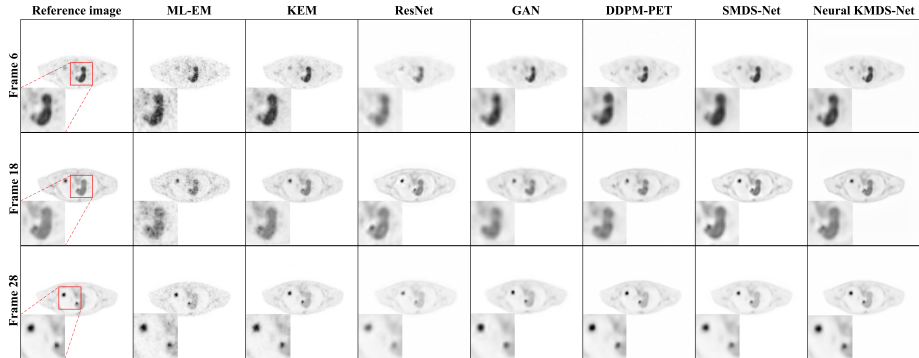


Figure 7: True activity images and denoised images by different methods in the clinical study. The window size of frame 6 (top row), frame 18 (middle row) and frame 28 (bottom row) is set to $[0, 0.1]$, $[0, 0.15]$ and $[0, 0.8]$, respectively. Each image is shown in a transverse view.

the value from the set of $\{64, 128\}$. I_3 is chosen from the set of $\{4, 8\}$. I_4 is changed from 12 to 32 with an interval of 4. When $I_1 = I_2 = 64$ and $I_3 = 4$, the stride of the first convolutional layer in Λ and Γ is set to 2 and the first layer in Φ and Ψ is replaced with a transposed convolutional layer. As shown in Table 5, using larger I_1 , I_2 , I_3 and I_4 enhance the representation ability of neural KMDS-Net and achieve better denoising performance. However, increasing I_4 from 24 to 32, the denoising performance changes are not significant. This is also consistent with the constraints on the size of β in (3).

4. Real patient study

4.1. Data acquisitions

We further employ neural KMDS-Net for dynamic PET denoising for real patient datasets. 65 patients scans are performed using the DigitMI 930 PET/CT system. The acquisition starts right after the injection of $1.85 \sim 4.44$ MBq/kg ^{18}F -FDG and lasts 60

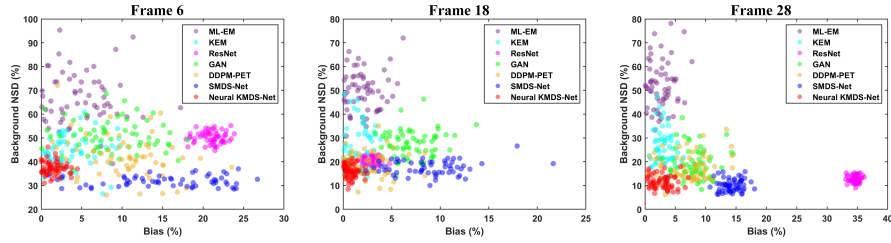


Figure 8: Plots of bias of tumor (frame 6 and 28) and cardiac (frame 18) versus cardiac background NSD. Each point represents the evaluation result from a realization of the test reference image in Fig. 7.

Table 6: Quantitative comparison of the global chest image for frame 6, 18 and 28 using PSNR and SSIM in the clinical study. Mean is reported. Best results are marked in **BOLD**.

Methods	ML-EM	KEM	ResNet	GAN	DDPM-PET	SMDS-Net	Neural KMDS-Net
PSNR							
Frame 6	25.795	28.702	25.580	30.826	31.908	32.403	33.081
Frame 18	28.238	31.717	31.449	32.532	33.603	33.125	35.289
Frame 28	33.297	35.237	32.512	37.164	37.460	37.748	40.795
SSIM							
Frame 6	.645	.741	.746	.822	.847	.883	.884
Frame 18	.735	.843	.867	.869	.897	.927	.934
Frame 28	.811	.870	.898	.924	.928	.948	.963

minutes. Fifty-five patient data are used for training, while the remaining ten patient data are used for testing. Informed consent is obtained from all human subjects involved in this retrospective study. Approval of all ethical and experimental procedures and protocols is granted by the institutional review board of the Beijing Friendship Hospital, Capital Medical University, Beijing, China (approval number 2022-P2-314-01. date:10/08/2022). The one-hour data are divided into 28 time frames following the schedule $12 \times 60s$ and $16 \times 180s$. The original image matrix size is $192 \times 192 \times 96$ per bed position. Considering the limitations of GPU memory, the original image is continuously cropped along the third dimension into small block images of size $192 \times 192 \times 8$.

To generate the training data, the total acquired data is reconstructed as the label image using the vendor software. The acquired raw data is down-sampled to 1/10-th of the total counts and reconstructs as the input low-dose image. To increase the training data, 3 low-dose realizations from the high-dose data for each patient data are generated. For the test data, sixty noisy realizations for each patient data are simulated.

4.2. Results of denoised PET images

Fig. 7 shows the denoised chest PET images using different methods for frame 6, 18 and 28. All DL-based denoising models are trained exclusively using patients' chest PET data. The ML-EM has the highest noise and KEM effectively reduces image noise compared to ML-EM. ResNet and GAN successfully suppress the noise but introduce noticeable bias in the tumor and cardiac regions (Fig. 8), which similarly occurs in the results produced by SMDS-Net. DDPM-PET outperforms the above methods but introduces some textural details that are not present in the reference images. In comparison, the images denoised using the proposed neural KMDS-Net shows significant improvement with lower bias and noise. These observations are consistent with the quantitative results shown in Fig. 8 and Table 6.

To further evaluate the generalization of the data-driven denoising methods in clinical scenarios, we train the neural network models using whole-body PET data from multiple bed positions and validate them on brain data. Fig. 9 shows the denoised brain images using different methods for frame 6, 18 and 28. The ML-EM results suffer from heavy noise. The KEM suppresses noise well but still suffers from noise and artifacts due to insufficient kernel representation. ResNet produces severe bias and artifacts on all 3 frames. GAN, DDPM-PET and SMDS-Net produce poor results such as frame 6,

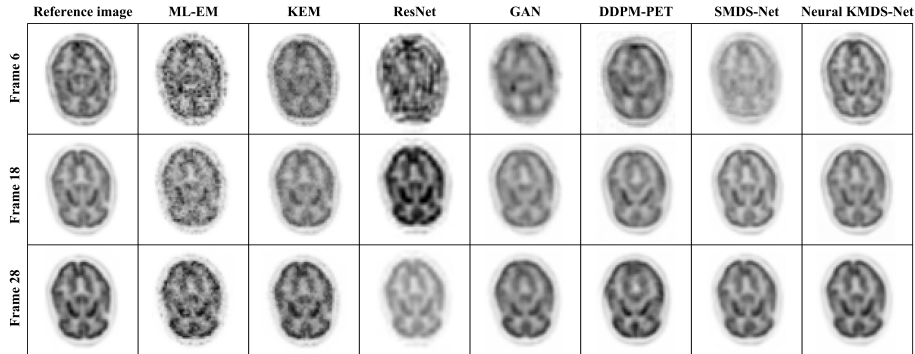


Figure 9: True activity images and denoised images by different methods in a clinical brain study. The window size of frame 6 (top row), frame 18 (middle row) and frame 28 (bottom row) is set to $[0, 0.04]$, $[0, 0.2]$ and $[0, 1]$, respectively. Each image is shown in a transverse view.

Table 7: Quantitative comparison of the global brain image for frame 6, 18 and 28 using PSNR and SSIM in the clinical study. Mean is reported. Best results are marked in **BOLD**.

Methods	ML-EM	KEM	ResNet	GAN	DDPM-PET	SMDS-Net	Neural KMDS-Net
PSNR							
Frame 6	28.564	34.267	18.720	30.760	31.405	27.910	35.257
Frame 18	30.578	36.391	23.275	34.062	31.350	34.886	37.985
Frame 28	31.348	35.994	26.054	34.626	31.879	36.787	38.788
SSIM							
Frame 6	.730	.883	.565	.787	.795	.716	.912
Frame 18	.839	.946	.898	.893	.830	.968	.971
Frame 28	.859	.944	.934	.915	.859	.968	.969

failing to preserve some structural contrast and details. In comparison, the images by the proposed neural KMDS-Net demonstrate a significant improvement with clearest structures and lowest noise. The quantitative results are shown in Table 7. Our method achieves the highest PSNR and SSIM, demonstrating that our proposed neural network has strong generalization capabilities compared to other deep learning methods.

5. Discussion

This paper develops a neural KMDS-Net algorithm for dynamic PET image denoising. The multidimensional sparse representation of the tensor is used to establish the spatial-temporal correlation of the 4D coefficient image in the kernel space for dynamic PET. A neural network is then utilized to facilitate adaptive parameter optimization. Compared with other DL-based methods, our network is a lightweight ($\sim 10\text{M}$) model with strong denoising capability for dynamic PET.

The tradeoff of bias and noise is challenging for dynamic PET image denoising. The model-based methods usually produce results with low bias and high noise. The DL-based methods, on the other hand, suppress noise significantly yet may introduce significant bias. Using deep learning modules in a physical model-driven solution may achieve a better tradeoff, but the denoising results may still be undesirable. Fully embedding deep learning priors into physical models may improve this issue. Therefore, in this paper, we construct a KMDS model in the image domain and substitute each module with a neural network, forming an end-to-end trainable neural network. Simulation and real results demonstrate that our approach produces promising results.

The main differences between our proposed method and SMDS-Net are as follows. I) The sparse coding space in which β sits. SMDS-Net uses a low-dimensional subspace to exploit the low-rankness, while we employ an isometric kernel space to establish spatial-temporal correlations for dynamic PET. It has been shown that the kernel method effectively leverages the prior knowledge of different frames in dynamic PET and may perform better in image denoising. II) The learnable parameters from (9) to (11). SMDS-Net uses dictionaries to explore the features and structures of tensors

in different dimensions. Our method uses convolutional kernels with stronger representation ability to optimize β . The sparse coding problem of β can be learned more accurately by neural networks.

Table 4 reveals that the performance of neural KMDS-Net is improved by stacking MDSB modules 20 times. However in the kernel representation module, stacking just two convolutional layers yields the optimal performance of neural KMDS-Net (as shown in Table 3). This illustrates the importance of physical model priors when designing neural network structures. We are considering integrating compressive sensing into the physical model, combining it with kernel methods and multidimensional sparse coding to design a better neural network architecture.

In the experiments with clinical data, it has been observed that the comparison methods like ResNet, GAN, DDPM-PET and SMDS-Net demonstrate good performance on later frames yet are quite poor on the earlier ones, showing severe artifacts or even distortion in the denoised PET images. This could be attributed to the fact that all frames are inputted into the network together, with short frames contributing less to the network’s total loss due to their low intensity values. In contrast, by implicitly integrating physical priors into the neural network, our proposed neural network has shown much better performance in the short frames, which is quite important for observing the tracer distribution close to the injection time.

In our generalization experiments, we utilize the network trained exclusively on dynamic PET whole-body data and test on brain dynamic PET sequences. The physical model-dependent approach such as KEM can effectively preserve image details but include significant noise. The deep learning methods, such as ResNet, GAN and

DDPM-PET, control noise well but tend to oversmooth the image details. In contrast, by designing neural networks based on physical models, our proposed neural KMDS-Net combines the high generalizability of the model-based methods with the strong denoising capabilities of DL-based methods. Incorporating more physical priors to guide the design of neural networks may further enhance the generalization performance of our model. In addition, we find that the neural network achieves the best performance when the acquisition time of test frame is similar to that of training frame. The network’s performance degrades when the acquisition time of the training and test data does not match. Therefore, to achieve optimal performance using the proposed neural KMDS-Net, a new refined training procedure may be needed when the noise levels of the test data differ from those of the training data.

The short frames in dynamic PET images are usually quite noisy due to the short frame durations, which makes denoising more difficult. In this paper, we use kernel methods and multidimensional sparse tensors to establish in-depth relationship between temporal frames. Our future work will focus on using more advanced neural network structures in each optimization module to achieve better denoising results.

6. Conclusion

This paper proposes an end-to-end convolutional neural network designed based on a physical model to improve the quantitative accuracy of low-dose dynamic PET frames. In the methodology section, we detail the design principles for each module of the neural network architecture. In the experimental section, we determine the depth of network architecture and the size of network features through ablation studies. More-

over, all comparison methods are evaluated both qualitatively and quantitatively on simulated and clinical data. The proposed method demonstrates superior performance compared to all the benchmark approaches, particularly in the recovery of low-dose frames.

Benefiting from the neural network architecture guided by the physical model, our method enables the rapid acquisition of high-quality dynamic PET images in clinical scenarios. Furthermore, the application of our method may be extended to various imaging scenarios such as hyperspectral imaging. However, despite its promising performance, the proposed method still has potential for further enhancement. (1) Convolutional layers are used to replace several steps in the optimization process of the denoising model. Future work will include using more advanced network mechanisms such as spatial-temporal joint attention. (2) Only the kernel method and multidimensional sparse coding are integrated in designing the neural network. The denoising performance may be further improved by incorporating more explainable strategies such as compressed sensing. (3) The optimal network parameters are numerically determined through experiments. In future work, they may be automatically adjusted in a more learnable manner. (4) In clinical scenarios, the performance of the algorithm may be affected when the noise distribution changes significantly, which needs to be explored in our future studies.

7. CRediT authorship contribution statement

Xiaodong Kuang: Conceptualization, Methodology, Software, Validation, Formal analysis, Writing - Original Draft. **Bingxuan Li:** Methodology, Visualization. **Yuan**

Liu: Visualization, Software. **Fan Rao:** Data Processing, Software. **Gege Ma:** Validation, Visualization. **Qingguo Xie:** Data Acquisition, Writing–Editing. **Greta S P Mok:** Conceptualization, Methodology, Writing – Review. **Huafeng Liu:** Result Analysis, Writing – Review. **Wentao Zhu:** Conceptualization, Methodology, Writing – Review, Supervision, Funding acquisition.

8. Declaration of competing interest

The authors declare that they have no known competing financial interests or personal relationships that could have appeared to influence the work reported in this paper.

9. Acknowledgments

This work was supported by the National Natural Science Foundation of China under Grant 62001425.

References

- [1] Jinyi Qi and Richard M Leahy. Iterative reconstruction techniques in emission computed tomography. *Physics in Medicine and Biology*, 51:541–578, 2006.
- [2] P.J. Green. Bayesian reconstructions from emission tomography data using a modified em algorithm. *IEEE transactions on medical imaging*, 9:84–93, 1990.
- [3] Lijun Lu, Nicolas A Karakatsanis, Jing Tang, Wufan Chen, and Arman Rahmim. 3.5 d dynamic pet image reconstruction incorporating kinetics-based clusters. *Physics in Medicine and Biology*, 57:5035, 2012.

- [4] Claude Comtat, Paul E Kinahan, Jeffrey A Fessler, Thomas Beyer, David W Townsend, Michel Defrise, and Christian Michel. Clinically feasible reconstruction of 3d whole-body pet/ct data using blurred anatomical labels. *Physics in Medicine and Biology*, 47:1, 2001.
- [5] Guobao Wang and Jinyi Qi. Pet image reconstruction using kernel method. *IEEE Transactions on Medical Imaging*, 34:61–71, 2015.
- [6] Hsuan-Ming Huang. Dynamic pet reconstruction using the kernel method with non-local means denoising. *Biomedical Signal Processing and Control*, 68:102673, 2021.
- [7] Ju-Chieh Kevin Cheng, Connor Bevington, Arman Rahmim, Ivan Klyuzhin, Julian Matthews, Ronald Boellaard, and Vesna Sossi. Dynamic pet image reconstruction utilizing intrinsic data-driven hypr4d denoising kernel. *Medical physics*, 48:2230–2244, 2021.
- [8] A. Buades, B. Coll, and J.-M. Morel. A non-local algorithm for image denoising. *2005 IEEE Computer Society Conference on Computer Vision and Pattern Recognition*, 2:60–65, 2005.
- [9] Bradley T. Christian, Nicholas T. Vandehey, John M. Floberg, and Charles A. Mistretta. Dynamic pet denoising with hypr processing. *Journal of Nuclear Medicine*, 51:1147–1154, 2010.
- [10] Kostadin Dabov, Alessandro Foi, Vladimir Katkovnik, and Karen Egiazarian. Image denoising by sparse 3-d transform-domain collaborative filtering. *IEEE Transactions on image processing*, 16:2080–2095, 2007.

- [11] F. Hashimoto, H. Ohba, K. Ote, and H. Tsukada. Denoising of dynamic sinogram by image guided filtering for positron emission tomography. *IEEE Transactions on Radiation and Plasma Medical Sciences*, 2:541–548, 2018.
- [12] Miho Shidahara, Yoko Ikoma, Jeff Kershaw, Yuichi Kimura, Mika Naganawa, and Hiroshi Watabe. Pet kinetic analysis: wavelet denoising of dynamic pet data with application to parametric imaging. *Annals of nuclear medicine*, 21:379–386, 2007.
- [13] Yuting Zhu, Qiang He, Yudong Yao, and Yueyang Teng. Self-supervised noise2noise method utilizing corrupted images with a modular network for ldct denoising. *Pattern Recognition*, 161:111285, 2025.
- [14] Huafeng Li Xiaoge He Dapeng Tao, Yuanyan Tang, and Ruxin Wang. Joint medical image fusion, denoising and enhancement via discriminative low-rank sparse dictionaries learning. *Pattern Recognition*, 79:130–146, 2018.
- [15] Qiong Liu, Yu-Jung Tsai, Jean-Dominique Gallezot, Xueqi Guo, Ming-Kai Chen, et al. Population-based deep image prior for dynamic pet denoising: A data-driven approach to improve parametric quantification. *Medical Image Analysis*, 95:103180, 2024.
- [16] Abolfazl Mehranian, Scott D. Wollenweber, Matthew D. Walker, Kevin M. Bradley, Patrick A. Fielding, Kuan-Hao Su, Robert Johnsen, Fotis Kotasidis, Floris P. Jansen, and Daniel R. McGowan. Image enhancement of whole-body oncology [18f]-fdg pet scans using deep neural networks to reduce noise. *European journal of nuclear medicine and molecular imaging*, 49:539–549, 2022.

- [17] Tzu-An Song, Samadrita Roy Chowdhury, Fan Yang, and Joyita Dutta. Pet image super-resolution using generative adversarial networks. *Neural Networks*, 125:83–91, 2020.
- [18] Zhengyu Peng, Fanwei Zhang, Han Jiang, Guichao Liu, Jingzhang Sun, Yu Du, Zhonglin Lu, Ying Wang, and Greta S. P. Mok. Deep learning-based low count whole-body positron emission tomography denoising incorporating computed tomography priors. *Quantitative Imaging in Medicine and Surgery*, 14:8140154–8148154, 2024.
- [19] Long Zhou, Joshua D. Schaefferkoetter, Ivan W.K. Tham, Gang Huang, and Jianhua Yan. Supervised learning with cycleGAN for low-dose fdg pet image denoising. *Medical image analysis*, 65:101770, 2020.
- [20] Kuang Gong, Keith Johnson, Georges El Fakhri, Quanzheng Li, and Tinsu Pan. Pet image denoising based on denoising diffusion probabilistic model. *European Journal of Nuclear Medicine and Molecular Imaging*, 51:358–368, 2024.
- [21] Siqi Li and Guobao Wang. Deep kernel representation for image reconstruction in pet. *IEEE Transactions on Medical Imaging*, 41:3029–3038, 2022.
- [22] Siqi Li, Kuang Gong, Ramsey D. Badawi, Edward J Kim, Jinyi Qi, and Guobao Wang. Neural kem: A kernel method with deep coefficient prior for pet image reconstruction. *IEEE Transactions on Medical Imaging*, 42:785–796, 2022.
- [23] Xiaodong Kuang, Bingxuan Li, Tianling Lyu, Yitian Xue, Hailiang Huang, Qingguo Xie, and Wentao Zhu. Pet image reconstruction using weighted nuclear norm maximization and deep learning prior. *Physics in Medicine and Biology*, 2024.

- [24] Qiyang Zhang, Yingying Hu, Yumo Zhao, Jing Cheng, Wei Fan, and Debin Hu. Deep generalized learning model for pet image reconstruction. *IEEE Transactions on Medical Imaging*, 43:122–134, 2023.
- [25] Fengchao Xiong, Jun Zhou, Shuyin Tao, Jianfeng Lu, Jiantao Zhou, and Yuntao Qian. Smds-net: Model guided spectral-spatial network for hyperspectral image denoising. *IEEE Transactions on Image Processing*, 31:5469–5483, 2022.
- [26] Na Qi, Yunhui Shi, Xiaoyan Sun, and Baocai Yin. Tensr: Multi-dimensional tensor sparse representation. *Proceedings of the IEEE conference on computer vision and pattern recognition*, pages 5916–5925, 2016.
- [27] Wei He, Quanming Yao, Chao Li, Naoto Yokoya, Qibin Zhao, Hongyan Zhang, and Liangpei Zhang. Non-local meets global: An iterative paradigm for hyperspectral image restoration. *IEEE Transactions on Pattern Analysis and Machine Intelligence*, 44:2089–2107, 2020.
- [28] Sergey Ioffe and Christian Szegedy. Batch normalization: Accelerating deep network training by reducing internal covariate shift. *arXiv preprint arXiv:1502.03167*, 2015.
- [29] Kaiming He, Xiangyu Zhang, Shaoqing Ren, and Jian Sun. Deep residual learning for image recognition. *Proceedings of the IEEE conference on computer vision and pattern recognition*, pages 770–778, 2016.
- [30] Phillip Isola, Jun-Yan Zhu, Tinghui Zhou, and Alexei A. Efros. Image-to-image translation with conditional adversarial networks. *Proceedings of the IEEE conference on computer vision and pattern recognition*, pages 1125–1134, 2017.

- [31] Xiaodong Kuang, Jianfei Zhu, Xiubao Sui, Yuan Liu, Chengwei Liu, Qian Chen, and Guohua Gu. Thermal infrared colorization via conditional generative adversarial network. *Infrared Physics and Technology*, 107:10338, 2020.
- [32] Chitwan Saharia, William Chan, Huiwen Chang, et al. Palette: Image-to-image diffusion models. *ACM SIGGRAPH 2022 conference proceedings*, pages 1–10, 2022.